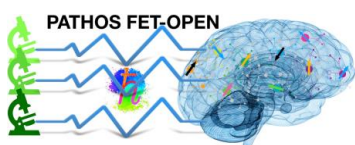


PHOTONIC AND NANOMETRIC HIGH-SENSITIVITY BIO-SENSING

DELIVERABLE 3.5 [HUJI, M12] REPORT ON NV IMAGER





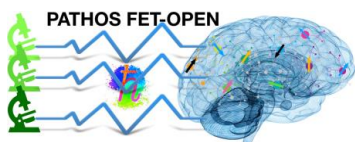
NV IMAGER

Work Package 3

Prof. Nir Bar-Gill, Hebrew University, Jerusalem, Israel

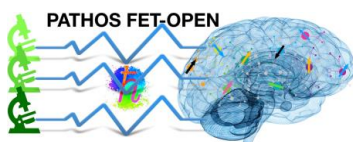
Project number: 828946

Project partners: UNIFI, Weizmann, INRiM, HUJI, TUDO



Contents

1	Executive Summary.....	5
2	NV magnetic sensing background.....	6
2.1	NV fundamentals.....	6
2.1.1	physical structure and formation.....	6
2.1.2	Electronic structure.....	6
2.2	NV center magnetometry.....	8
2.2.1	NV center in magnetic field.....	8
2.2.2	Hyperfine coupling with Nitrogen.....	9
2.2.3	ODMR measurement.....	9
2.2.4	vector magnetometry.....	12
2.2.5	Sensitivity.....	13
3	Widefield Magnetic imaging.....	15
3.1	Experimental Setup.....	15
3.1.1	General description of the system.....	15
3.1.2	Biased magnetic field.....	16
3.1.3	Diamond sample.....	18
3.2	Measurement protocols.....	18
3.2.1	Method 1: cw-ODMR with high MW power.....	20
3.2.2	Method 2: cw-ODMR with low MW power, sweeping with 2 MW frequencies simultaneously.....	22
3.3	Test measurement-Magnetic image of a field formed by wire.....	23
4	Magnetic imaging demo.....	26
4.1	Paleomagnetism introduction.....	26
4.2	Other measurement methods.....	26
4.3	Measuring rock samples with NV center.....	26
4.4	Rock measurement protocol.....	27
4.5	Results.....	28
4.5.1	Multi-domain measurements results.....	28
4.5.2	Dipole measurements results.....	28
4.6	Future capabilities and applications.....	30
5	Reference.....	31

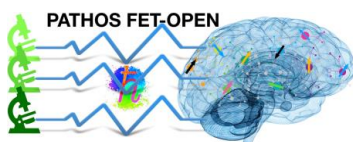


1 Executive Summary

As part of Deliverable 3.5 [M12], we have constructed a general-purpose nitrogen-vacancy (NV) magnetic imager. This setup is capable of various NV magnetic measurements, demonstrated below, as well as the characterization and study of NV properties, system and bath control schemes and additional techniques, tools and fundamental aspects related to the project.

We detail in this report the NV magnetic imager system and its capabilities. We demonstrate these capabilities on a few example magnetic sensing scenarios. Moreover, we demonstrate fundamental studies of control techniques relevant to this project enabled by this system.

The reported deliverable forms a crucial step toward the realization of the objectives of this project, as it serves as a versatile platform for the further experiment planned herein.



2 NV magnetic sensing background

2.1 NV fundamentals

2.1.1 physical structure and formation

The nitrogen-vacancy (NV) center is a point defect in the diamond's lattice with C_{3V} symmetry. It consists of a substitutional nitrogen atom adjacent to a carbon vacancy that is oriented along one of the four crystalline directions $[111]$ [see Figure 1]. These four NV orientations are usually equally populated in a bulk diamond. The NV center is known to exist in negative NV^- and neutral NV^0 charge state. The NV^- charge state, which is believed to receive its additional electron from a nearby substitutional nitrogen atom, is the charge state which possesses the useful properties we exploit in this work. The NV center can be found as a product of the following procedures: 'in grown' product of the chemical vapour deposition (CVD) process; as a product of radiation damage and annealing; and ion implantation and annealing, in bulk and nanocrystalline diamond. In this work, we use a CVD diamond containing NV centers in bulk, created by ion implantation and annealing.

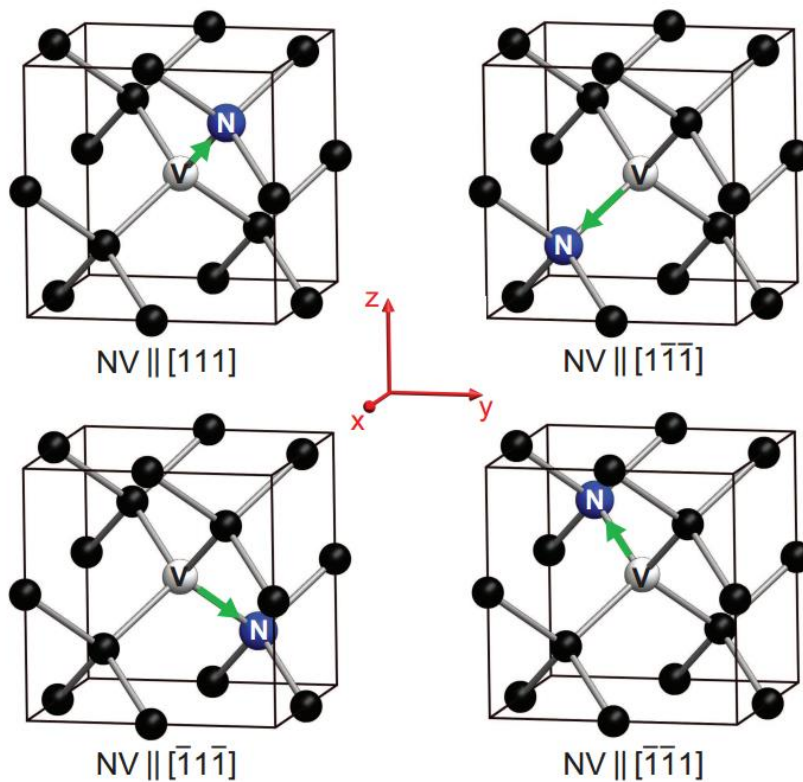
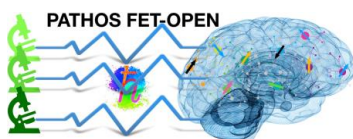


Figure 1: Four orientations of the NV center in a diamond. [Four orientations of the NV center in a diamond. Carbon atoms are depicted in black, nitrogen (N) atoms in blue, and vacancies (V) in white. The NV electronic spin is indicated by green arrows.]

2.1.2 Electronic structure



The NV center is a spin triplet in the electronic ground state, where the degenerated $m_s = \pm 1$ sublevel states are separated from the $m_s = 0$ state by 2.87 GHz due to spin-spin interactions. When a small external magnetic field is applied along the NV symmetry axis, the degeneracy of the $m_s = \pm 1$ energy levels is lifted via Zeeman splitting, which can be written as $\Delta = 2 \gamma B_{\parallel}$, where $\gamma = 28$ GHz/Tesla represents the electronic gyromagnetic ratio and B_{\parallel} is the external magnetic field along the NV center symmetry axis [see Figure 2].

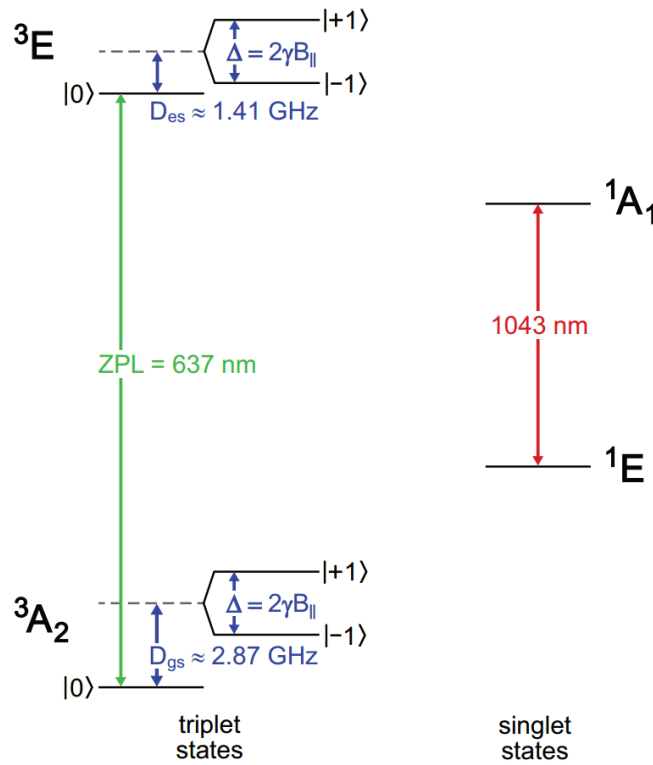
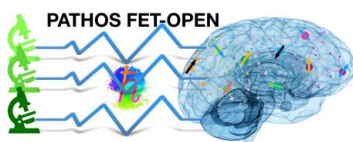


Figure 2: NV center electronic energy level structure at room temperature. The ground state is a spin triplet with a zero field splitting, $D_{gs} = 2.87$ GHz. The excited state, which is also a spin triplet with a zero field splitting, $D = 1.41$ GHz, separated by 637 nm from the ground state. The degeneracy of the spin $m_s = \pm 1$ levels is lifted via Zeeman splitting, Δ , due to the external magnetic field along the NV symmetry axis. The singlet states are separated by a 1043 nm.

As shown in Figure 2, spin preserving optical transitions between the ground (3A_2) and excited (3E) triplet states, have a characteristic zero-phonon line (ZPL) at 637 nm with a broad phonon-sideband of 640 – 800 nm at room temperature. An alternative, non-radiative decay through the (1A) singlet state enable spin population transitions from $m_s = \pm 1$ states to the $m_s = 0$ state. As a result, when the NV center is excited in the $m_s = 0$ state, it exhibits a high fluorescence rate. In contrast, when the NV center is excited in the $m_s = \pm 1$ states, the NV center has a higher probability to cross over to the non-radiative decay path, which exhibits low fluorescence. In addition, continuous optical excitation will eventually pump the NV center into the $m_s = 0$ state with polarization degree of 80 – 95%.



2.2 NV center magnetometry

2.2.1 NV center in magnetic field

As mentioned before, the NV center has a spin-triplet ground state with a 2.87 GHz zero-field splitting between the 0 and $m_s = \pm 1$ states. Therefore, the Hamiltonian of NV center in magnetic field can be written as

$$H = D_{gs}S_z^2 + \gamma B_{\parallel}S_z + \gamma B_{\perp}S_x + H_{strain} \quad (1)$$

Where $D_{gs} = 2.87 \text{ GHz}$ denotes the crystal field amplitude and $\gamma = 28 \text{ GHz/Tesla}$ representing the electronic gyromagnetic ratio. B_{\parallel} and B_{\perp} representing the external magnetic field projection parallel and perpendicular to the NV center symmetry axis respectively and H_{strain} is the energy shift induced by local strain. In addition S_x , S_y and S_z are the spin operators, which can be written as:

$$S_x = \frac{1}{\sqrt{2}} \begin{bmatrix} 0 & 1 & 0 \\ 1 & 0 & 1 \\ 0 & 1 & 0 \end{bmatrix}, S_y = \frac{1}{i\sqrt{2}} \begin{bmatrix} 0 & 1 & 0 \\ 1 & 0 & 1 \\ 0 & 1 & 0 \end{bmatrix}, S_z = \begin{bmatrix} 1 & 0 & 0 \\ 0 & 0 & 0 \\ 0 & 0 & -1 \end{bmatrix} \quad (2)$$

The term $\gamma B_{\parallel}S_z$ in the Hamiltonian caused an even linear Zeeman splitting of $m_s = \pm 1$ states relative to the $m_s = 0$ state and the term $\gamma B_{\perp}S_x$ caused a nonlinear Zeeman splitting. The effect of $\gamma B_{\perp}S_x$ can be divide into two. First, even nonlinear energy splitting of $m_s = \pm 1$ states relative to the $m_s = 0$ state. Secondly, energy shifting of $m_s = \pm 1$ states relative to the $m_s = 0$ state. Now we will see how these effects influence the resonance NV spin transitions of $m_s = 0$ state to $m_s = +1$ and $m_s = -1$ states. based on Equations 1 and 2, using perturbation theory (assuming $\gamma B_{\perp} \ll D_{gs}$), we can write the energy levels and the energy resonance NV spin transitions up to the second order:

$$\Delta_{1,0} = D_{gs} \left[1 + \frac{\gamma B_{\parallel}}{D_{gs}} + \frac{3(\gamma B_{\perp})^2}{2(D_{gs}^2 - \gamma B_{\parallel}^2)} - \left(\frac{\gamma B_{\parallel}}{D_{gs}} \right) \frac{(\gamma B_{\perp})^2}{2(D_{gs}^2 - \gamma B_{\parallel}^2)} O(\gamma B_{\perp})^3 \right] + a_{strain}^{1,0} \quad (3)$$

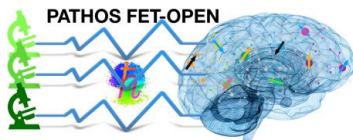
$$\Delta_{-1,0} = D_{gs} \left[1 - \frac{\gamma B_{\parallel}}{D_{gs}} + \frac{3(\gamma B_{\perp})^2}{2(D_{gs}^2 - \gamma B_{\parallel}^2)} + \left(\frac{\gamma B_{\parallel}}{D_{gs}} \right) \frac{(\gamma B_{\perp})^2}{2(D_{gs}^2 - \gamma B_{\parallel}^2)} + O((\gamma B_{\perp})^3) \right] + a_{strain}^{-1,0} \quad (4)$$

Where in both Equations 3 and 4, the first term is the Zero field splitting, the second term is responsible to the even linear Zeeman splitting, the third term creates the energy shifting, the fourth term responsible to the even nonlinear energy splitting and both $a_{strain}^{1,0}$ and $a_{strain}^{-1,0}$ represent the strain effects. If we work with small magnetic fields (also $\gamma B_{\parallel} \ll D_{gs}$ in addition to $\gamma B_{\perp} \ll D_{gs}$) the even nonlinear energy splitting term have a small contribution to the resonance transition (third order effect) and therefore can be disregard. As a result, under these assumptions, we can associate the difference between the energy resonance spin transitions to γB_{\parallel} alone (up to the second order strain effects) so we can find the external magnetic field projection along the NV center symmetry axis using:

$$B_{\parallel} = (\Delta_{1,0} - \Delta_{-1,0})/2\gamma \quad (5)$$

In case $B_{\parallel} \sim B_{\perp}$ we have $\frac{3(\gamma B_{\perp})^2}{2(D_{gs}^2 - \gamma B_{\parallel}^2)} \ll \frac{\gamma B_{\parallel}}{D_{gs}}$ in Equations 3 and 4, it is enough to use one energy resonance transition in order to find the external magnetic field (up to the strain effects):

$$B_{\parallel} = (\Delta_{1,0} - D_{gs})/\gamma = (\Delta_{-1,0} - D_{gs})/\gamma \quad (6)$$



In order to eliminate the influence of the strain effects on the measurement of the magnetic field it is possible to perform a reference measurement namely, performing an additional measurement without the wanted magnetic field and subtract it from the actual measurement.

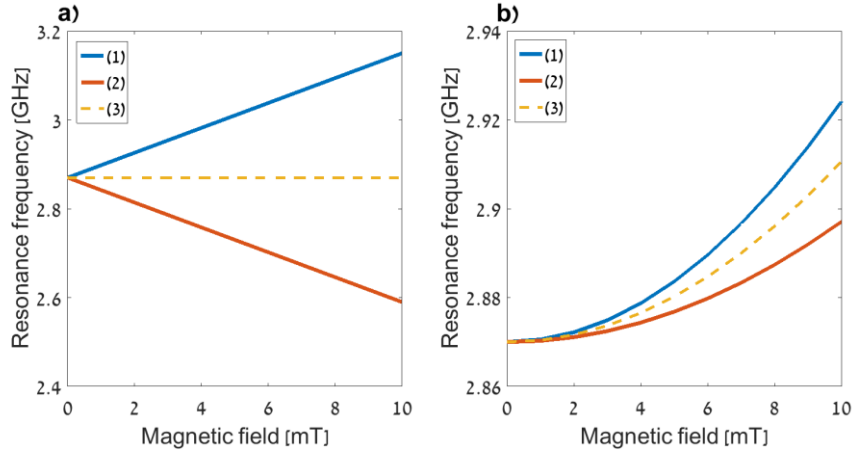


Figure 3 : Spin transition frequencies vs external magnetic field simulation based on Equation 1 with an external magnetic field parallel (a) and perpendicular (b) to the NV center symmetry axis. The blue curve (1) and the red curve (2) represent the resonance transitions between 0 and +1, and between 0 and -1, respectively. The yellow curve represents the middle frequency between the two transitions.

2.2.2 Hyperfine coupling with Nitrogen

The small anisotropic component of the NV- hyperfine interaction can be explained from dipolar interaction between the nitrogen nucleus and the unpaired-electron probability density localized on the three carbon atoms neighboring the vacancy. The hyperfine interaction Hamiltonian can be written as:

$$H_i = A_{\parallel} S_z I_z + A_{\perp} (S_x I_x + S_y I_y) \quad (7)$$

Where S , I denote electron and collective nuclear spin operators, respectively and A_{\parallel} and A_{\perp} are the axial and non-axial magnetic hyperfine parameters. For ^{14}N , $I = 1$ nuclear spin, $A_{\parallel} = 2.16 \text{ MHz}$, $A_{\perp} = 2.7 \text{ MHz}$ and for ^{15}N , $I = \frac{1}{2}$ nuclear spin, $A_{\parallel} = 3.1 \text{ MHz}$, $A_{\perp} = 3.1 \text{ MHz}$.

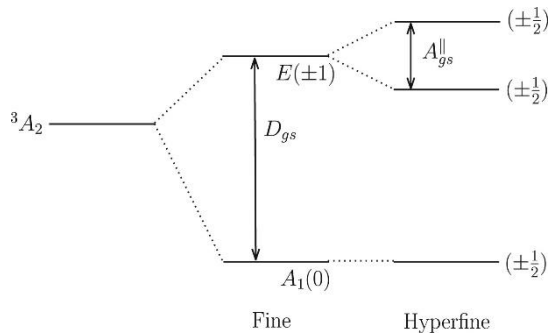
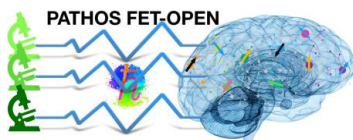


Figure 4: Fine and hyperfine structures of the 15NV- ground state. The fine structure levels are denoted by their spin-orbit symmetry and $m_s=0, \pm 1$ spin projections and the hyperfine structure levels are denoted by their $m_I=\pm 1/2, \pm 1$ spin projections.

2.2.3 ODMR measurement



In order to experimentally find the resonance NV spin transitions and measuring the external magnetic field we perform a continuous-wave optically detected magnetic resonance (cw ODMR). Simultaneous low intensity laser excitation (at 532 nm) and low power microwave (MW) radiation are applied and sweeping the frequency of the microwave field while monitoring the fluorescence intensity. When the MW frequency is off-resonant from all ground state spin transitions, the MW driving has no effect on the spin state and the laser excitation optically pumps the NV into the $m_s = 0$ spin state resulting in maximum fluorescence intensity. When the MW frequency is on-resonant with one of the resonance transitions, $m_s = 0$ to $m_s = +1$ and $m_s = 0$ to $m_s = -1$, the spin state cycles between $m_s = 0$ to $m_s = \pm 1$ states, resulting in fluorescence reduction. Using this spectrum and determining the fluorescence dips position the resonance NV spin transitions can be found and subsequently, the magnetic field information can be extracted.

In order to infer the behavior of the contrast and the line-width of the cw ODMR as a function of the microwave and the optical pumping power we consider the NV defect as a simple closed two-level system, denoted 0 and 1 respectively corresponding to the ground states with spin projection $m_s = 0$ and $m_s = -1$. In this simple model the Hamiltonian describing the interaction of the system with the driving MW radiation and the laser excitation under DC magnetic field can be read as:

$$H = \omega_0 11 + \Omega_R \cos(\omega_m t)(01 + 10) \quad (8)$$

where ω_0 is the resonance transition frequency caused by the crystal field amplitude and the external magnetic field, Ω_R is the Rabi frequency of the magnetic dipole interaction and ω_m is the driving MW frequency.

Using the formalism of the density operator σ the evolution of the system is then described by the Liouville equation:

$$\dot{\sigma} = -i[H, \sigma] + L_{relax} \quad (9)$$

The last term describes the relaxation of the system through its interaction with the environment and the optical pumping. In this model we use the intrinsic relaxation of the populations σ_{ii} occurs through a spin-lattice relaxation process with a rate denoted by Γ_1 , while the coherences σ_{ij} decay with an inhomogeneous dephasing rate Γ_2^* . Within this simplified framework, we do not consider populations either in the excited state or in the metastable state. The effect of optical pumping is thus phenomenologically introduced through an induced relaxation process, both for populations and coherences. The effect of the metastable state responsible for spin polarization is described by a relaxation process of the population σ_{11} with a polarization rate given by:

$$\Gamma_p = \Gamma_p^\infty \frac{s}{s+1} \quad (10)$$

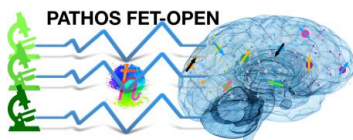
where $s = \mathcal{P}_{opt}/\mathcal{P}_{sat}$ is the saturation parameter of the radiative transition, \mathcal{P}_{opt} and \mathcal{P}_{sat} are the optical pumping power used in the experiment and the saturation pumping power respectively and $\Gamma_p^\infty = 5 \times 10^6 \text{ s}^{-1}$ is the polarization rate at saturation. The relaxation rate of the electron spin coherences σ_{ij} induced by optical pumping can be written as

$$\Gamma_c = \Gamma_c^\infty \frac{s}{s+1} \quad (11)$$

where $\Gamma_c^\infty = 8 \times 10^7 \text{ s}^{-1}$ is the rate of optical cycles at saturation. This quantity is set by the excited-state radiative lifetime. Substitute these rates into the relaxation term in equation 9 with the correct operators gives the following rate equations system.

$$\frac{d\sigma_{1,1}}{dt} = i \frac{\Omega_R}{2} [\sigma_{1,0} - \sigma_{0,1}] - \Gamma_1 [\sigma_{1,1} - \sigma_{0,0}] - \Gamma_p \sigma_{1,1} \quad (12)$$

$$\frac{d\sigma_{0,1}}{dt} = i[\omega_m - \omega_0]\sigma_{0,1} - i \frac{\Omega_R}{2} [\sigma_{1,1} - \sigma_{0,0}] - \Gamma_2 \sigma_{0,1} \quad (13)$$



where $\Gamma_2 = \Gamma_2^* + \Gamma_c$. The steady-state solutions of the populations $\sigma_{1,1}^{st}$ are then given by

$$\sigma_{1,1}^{st} = \frac{\frac{\Gamma_1}{2\Gamma_1 + \Gamma_p}([\omega_0 - \omega_m]^2 + \Gamma_2^2) + \frac{\Gamma_2 \Omega_R / 2}{2\Gamma_1 + \Gamma_p}}{[\omega_0 - \omega_m]^2 + \Gamma_2^2 + \frac{\Gamma_2 \Omega_R}{2\Gamma_1 + \Gamma_p}} \quad (14)$$

$$\sigma_{0,0}^{st} = 1 - \sigma_{1,1}^{st} \quad (15)$$

Using Equations 10,11 assuming the steady state solution from Equations 14 and 15 the NV center fluorescence can be written as:

$$I(\Omega_R, \omega_m, s) = [\alpha \sigma_{0,0}^{st} + \beta \sigma_{1,1}^{st}] \times \frac{s}{s+1} \times I^\infty \quad (16)$$

Where the parameters $\alpha \approx 0.72$ and $\beta \approx 0.28$ are phenomenologically introduced in order to account for the difference in the fluorescence intensity rate between the $m_s = 0$ and $m_s = 1$ spin sublevels ($\alpha > \beta$) and $I^\infty \approx 7.7 \times 10^7 \text{ s}^{-1}$ is the fluorescence intensity rate at saturation. Using the above notation, the ODMR contrast can then be evaluated as

$$C(\Omega_R, \omega_m, s) = \frac{I(0,0,s) - I(\Omega_R, \omega_m, s)}{I(0,0,s)} \quad (17)$$

where $I(0,0,s)$ (respectively $I(\omega_R, \omega_m, s)$) denotes the NV defect PL without applying the microwave field (respectively with a microwave field).

Finally using Equations 14-17 one can calculate the ODMR contrast as function of the microwave power, Ω_R , the microwave frequency, ω_m and the laser pumping ratio, s .

Based on Equation 17 we can understand the outcome contrast better and estimate the required MW and the optical pumping power in order to get the best measurement in terms of magnetic sensitivity and minimum detectable magnetic field. In Figure 5 it is possible to see the contrast function behavior at different driving parameters (s and Ω_R) where both, the FWHM and the maximum contrast are changed. For more detailed behavior of the FWHM and the maximum contrast of the ODMR see Figure 6. These functions present a non-monotonic complex behavior over the typical span of MW and laser power. therefore, it is useful to determine the right parameters using Equation 17 to maximize the FWHM and the maximum contrast in order to get the most accurate resonance measurement.

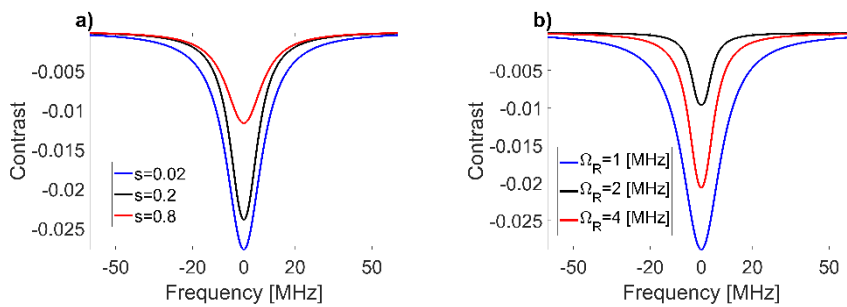
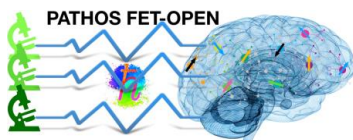


Figure 5: Simulation results based on Equation 17 at different parameters assuming NV with 15N. (a) ODMR simulation in various saturation parameters with MW power value of $\Omega_R = 2.5 \text{ MHz}$. (b) ODMR simulation in various MW power parameters with saturation value of $s = 0.2$.



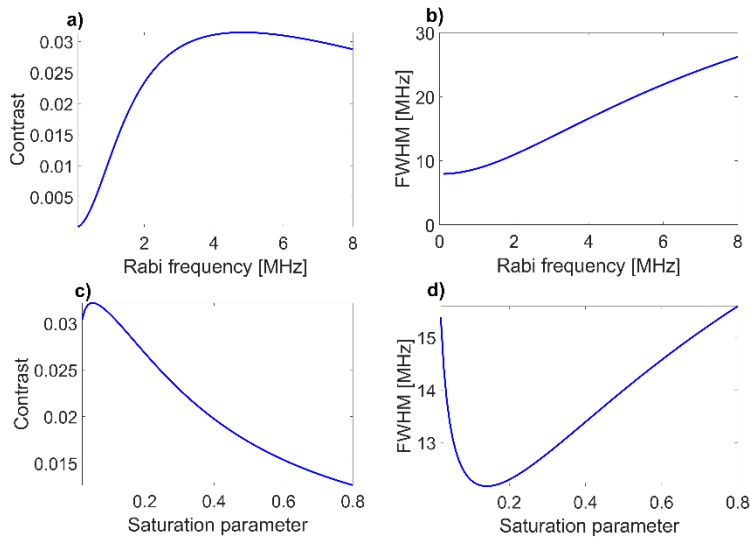


Figure 6: The ODMR contrast and the FWHM behavior as function of the saturation parameter and the MW power assuming NV with 15N. (a),(b) The ODMR contrast and FWHM as function of the Rabi frequency, when the saturation parameter is 0.2. (c),(d) The ODMR contrast and FWHM as function of the saturation parameter, when the saturation Rabi frequency is 2.5.

At low enough laser intensity and MW power, it is also possible to resolve the splitting due to Fermi contact hyperfine interactions between the NV electronic spin and the nuclear spin associated with the N in the NV complex [Figure 7].

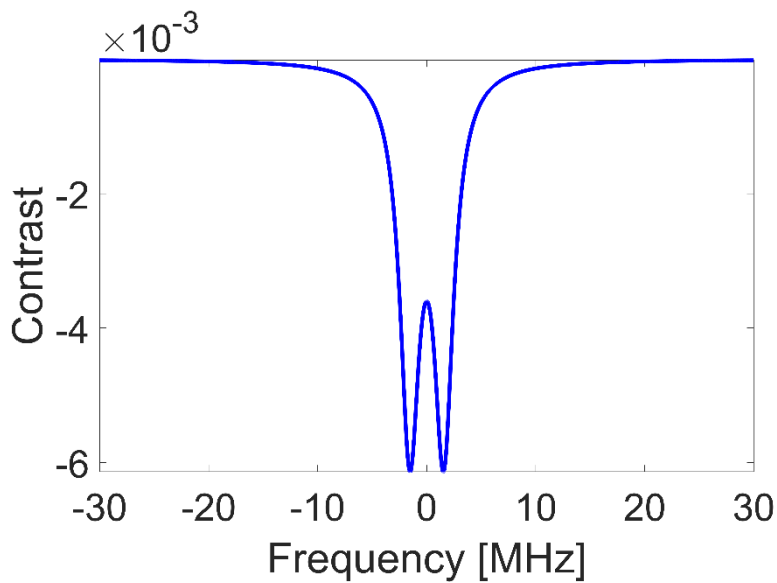
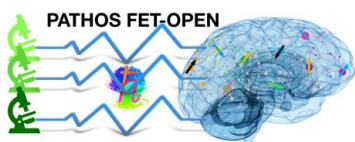


Figure 7: Simulation results based on Equation 17 at relatively low MW power and laser intensity, $\Omega_R=0.2\text{MHz}$. and $s=0.02$ assuming NV with 15N.

2.2.4 vector magnetometry



As mentioned before, the NV center can be found in four crystallographic direction ($[111]$, $[1\bar{1}1]$, $[1\bar{1}\bar{1}]$ and $[\bar{1}\bar{1}\bar{1}]$). Using the cw ODMR measurement we can measure the magnetic field along each NV orientation, and by transforming the tetrahedral directions into Cartesian coordinates we can reconstruct the vectorial magnetic field. Using simple geometric arguments to perform the tetrahedral- Cartesian transformation as defined in Figure 8, we find the following equations for the magnetic field components:

$$\begin{aligned} B_x &= \frac{\sqrt{3}}{2} (B_{o1} + B_{o3}) \\ B_y &= \frac{-\sqrt{3}}{2} (B_{o2} + B_{o3}) \\ B_z &= \frac{\sqrt{3}}{2} (B_{o1} + B_{o2}) \end{aligned} \quad (18)$$

Where, B_{oi} is the magnetic field along the i th NV orientation.

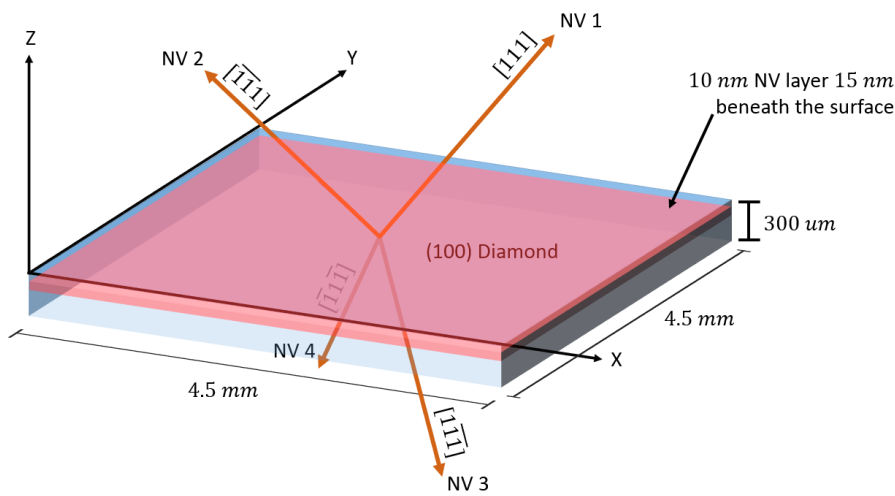


Figure 8: Schematic of sample orientations showing the (100) diamond surface (blue plane) and the four NV orientations (orange arrows). Crystallographic directions of the diamond are depicted as well as the Cartesian coordinate system.

2.2.5 Sensitivity

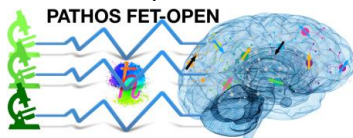
Consider an ODMR measurement of duration t_m , The number of photons collected per measurement is $N = I \times t_m$ where, I is the fluorescence rate given by Equation 16. The minimum detectable field for this measurement can be calculated by:

$$\Delta B_{min} = \frac{1}{\gamma} \min\{\Delta\omega_m\} = \frac{1}{\gamma} \min\left\{\frac{\Delta N}{|N\omega_m|}\right\} \quad (19)$$

Where B_0 is the projection of the magnetic field along the NV symmetry axis and the NV gyromagnetic ratio is $\gamma = 28$ MHz/T. Consider a measurement of duration t_m , the number of photons collected per measurement is $N = It_m$, where I is the fluorescence intensity rate. Assuming shot noise-limited measurement we can write:

$$\Delta B_{min} = \frac{1}{\gamma\sqrt{t_m}} \min\left\{\frac{\sqrt{I}}{|I\omega_m|}\right\} \quad (20)$$

The sensitivity of the ODMR measurement is then given by the following relation:



$$\eta_{ODMR} = \Delta B_{min} \sqrt{t_m} = \frac{1}{\gamma} \min\left\{\frac{\sqrt{I}}{|I\omega_m|}\right\} \quad (21)$$

The magnetic field sensitivity depends on the resonance contrast and the resonance linewidth through $I\omega_m$, the photons emission rate I and the gyromagnetic ratio $\gamma = 28 \text{ GHz/Tesla}$. The photons emission rate given by Equation 16 is depended on the intrinsic relaxation and inhomogeneous dephasing rate denoted by Γ_1 and Γ_2^* respectively, the MW power Ω_R and induced relaxation process Γ_c and Γ_p who depend on the laser pumping power. The cw-ODMR suffers from trade-offs; between power-broadening and lower contrast at higher optical powers and fewer photons collected per measurement at lower optical powers, and between lower contrast at lower MW powers and power-broadening at higher MW powers. Therefore, in order to receive the best magnetic sensitivity using the ODMR measurement we want to use a good diamond sample, with low Γ_2^* and Γ_1 parameters, in addition we need to find the optimal saturation parameter and the MW power.

For more realistic sensitivity assessment, it is necessary to take into account the fluorescence collection efficiency, CE ; the NV center density, ρ_{NV} ; the volume of which the NVs fluorescence contribute to the measurement, V , and the detector quantum efficiency, QE . Therefore the expression for the sensitivity in Equation 21 becomes:

$$\eta_{ODMR} = \Delta B_{min} \sqrt{t_m} = \frac{1}{\gamma} \min\left\{\frac{\sqrt{I}}{|I\omega_m|}\right\} \times \rho_{NV} V \times CE \times QE \quad (22)$$

Using the expression in Equation 22 we can estimate the expected sensitivity in a real measurement system as function of the laser and the MW power [see Figure 9] with typical parameters. The minimum sensitivity using the cw-ODMR method is around 1 T/Hz.

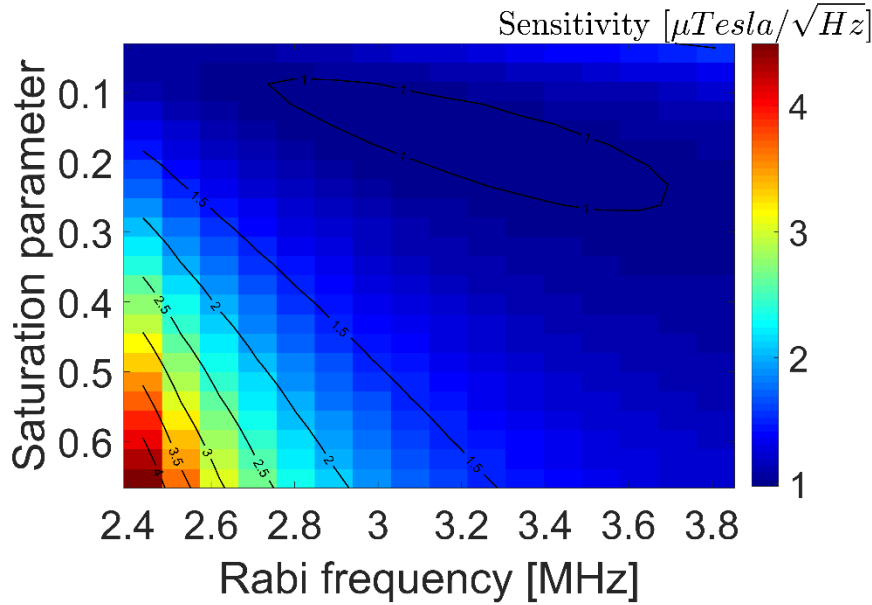
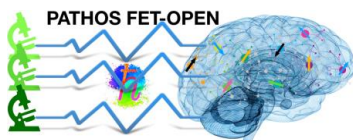


Figure 9: Two-dimensional plot of the magnetic field sensitivity simulation obtained by Equations 16 and 21 assuming NV with 15N. The solid lines correspond to isomagnetic field sensitivities. The simulation was done with the following typical parameters: $CE = 0.01$, $QE = 0.5$, $\rho_{NV} = 1.3 \times 10^{11} \text{ NV/cm}^2$, $V = 6.25 \times 10^{-8} \text{ cm}^2$



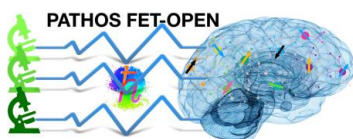
3 Widefield Magnetic imaging

In this chapter, we describe the methods for 2D imaging of magnetic fields using several measurements protocols based on cw-ODMR. To do this we used an ensemble of NV centers in a thin layer near the surface of a diamond chip, exciting NV centers confined to a thin surface layer over a large area in bulk diamond and imaging the resulting fluorescence onto a sCMOS camera. We demonstrate optical detection of 2D DC magnetic field patterns over a large field of view ($\sim 35 \times 35 \mu\text{m}$) with sub-micron spatial resolution and magnetic sensitivity of ~ 5 per pixel.

3.1 Experimental Setup

3.1.1 General description of the system

Magnetic measurements were performed using custom made wide-field fluorescence microscope [see Figure 10]. We used this system to perform 2-dimensional magnetic field imaging with thin-layer NV-diamond sample. Optical excitation obtained by a 532 nm laser (Laser Quantum Opus), which illuminates the region of interest inside the diamond, using EPI-illumination mode. The large field of view is achieved by a defocusing lens placed before the objective (Nikon), creating a field of view of $35 \mu\text{m}$. An acousto-optic modulator (AOM) (Isomet 1250C-848) is used as an optical switch, enabling the creation of light pulses which allow both manipulations and reading of the NV spin state. A loop antenna is located above the diamond surface, creating a homogeneous microwave field over the region of interest on the diamond. The MW antenna connects to a microwave generator (Agilent E8257D), amplified by an amplifier. Fast switching of the MW signal is achieved by a high isolation switch (ZASWA-2-50DR), enabling the coherent manipulation of the NV spin state necessary for an ODMR experiment. Optical and MW pulse timing are controlled by a computer-based digital delay generator (pinCore PulseBlaster PRO ESR500). The NV fluorescence is collected by the objective (Nikon CFI Plan Apo Lambda 60X/0.95) and filtered by a dichroic mirror (Semrock LM01-552-25) in MUX configuration, band pass filter and a notch filter. The fluorescence is imaged onto a sCMOS camera (Neo 5.5 sCMOS). Because the camera's minimum exposure time is larger than the single experiment duration, for a pulse experiment, the measurement is repeated for several thousand averages within a single exposure. The exposure time and the pulses are synchronized to an optical chopper (New Focus 3501) placed before the camera in order to block the fluorescence from the optical initialization pulses. A permanent magnet (K&J D88) is mounted on a 3-axis motorized stage in order to create the biased magnetic field, which removes the degeneracy of the different NV orientations. The whole system was controlled using a custom made MATLAB GUI.



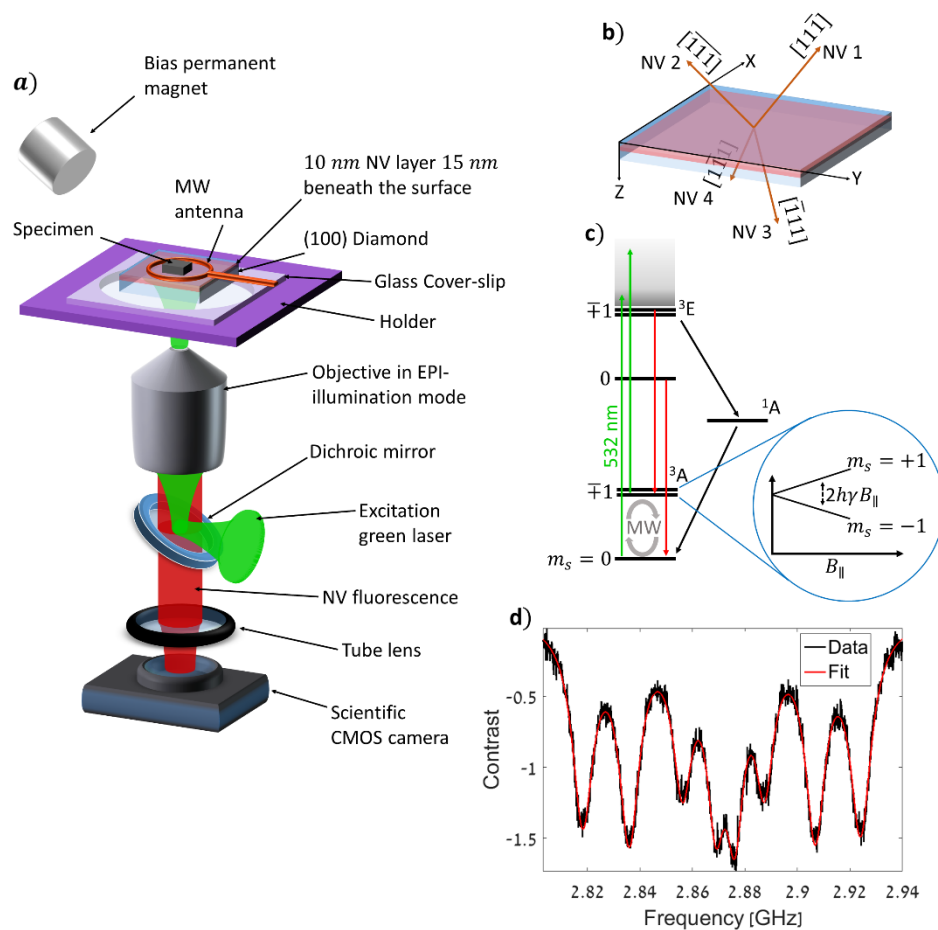
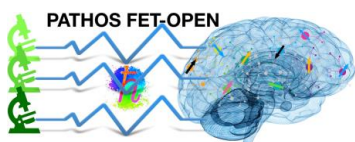


Figure 10: Schematic of the experiment, the NV structure and measurement process. (a) Custom-built Wide-field magnetic imaging microscope. The rock sample is placed on the surface of a diamond chip, which is implanted with a high density thin layer of nitrogen-vacancy (NV) centers near the surface. The diamond is attached to the cover-slip using immersion oil which is glued to the holder. Optical pumping green laser is incident through the bottom-polished side of the diamond surface using the objective in EPI mode. Coherent MW-field manipulation, which is created by an MW antenna, is located near the diamond surface containing the NV layer. The NV fluorescence passes through the diamond, the cover-slip and the dichroic mirror, and is then imaged onto the sCMOS camera using the objective and a tube lens. (b) Schematic of sample orientations showing the (100) diamond chip (blue) containing the NV layer (red) and the four NV orientations (orange arrows). Crystallographic directions of the diamond are depicted as well as the Cartesian coordinate system. (c), Energy-level diagram of the NV center. An external static magnetic field along the NV symmetry axis Zeeman-shifts the energy of the $m_s = \pm 1$ levels linearly (magnified on the right). (d), Full optically detected magnetic resonance (ODMR) spectra for one pixel. The characteristic dips correspond to the resonance transitions between the energy levels of the NV center's spin. Multiple resonances are observed, corresponding to the different NV orientations in the diamond crystal.

3.1.2 Biased magnetic field

We used three configurations to produce the biased magnetic field, depending on the measurement needs. In the next section we will present the all three configurations and their uses.

3.1.2.1 Helmholtz like permanent magnets configuration



When performing magnetic imaging over a wide field of view it is important to avoid spatial inhomogeneity of the biased magnetic field, which causes to a broadening in the frequency domain. To avoid this, we used two permanent magnets in a Helmholtz like configuration. We used two permanent ring magnets (model) posted one in front of the other in a distance such that the magnetic field in the middle between them is highly homogeneous. The first step was to create a simulation of a permanent magnet. For this we used a very useful toolbox of Mathematica called Radia. Using this toolbox, we simulated a cubic and a ring permanent magnets. The second part of the simulation creates two identical magnets and calculates the right distance between them to create the most homogeneous magnetic field. Finally, the last part of the simulation calculates the magnetic field at the middle and the magnetic field's homogeneity. we tried to simulate the Helmholtz like configuration with several magnet models from K&J and 'All' Magnets that will give us both the most homogeneous magnetic field and a magnetic field of ~ 30 Gauss (just enough to separate the energy gap of the four NV orientations). we found that the best result by far is the ring configuration. Using this method, with CR162 magnet from All Magnets, we received the following results: a magnetic field of 37 Gauss and an homogeneity of 5.7×10^{-3} Gauss (the maximum change of the magnetic field in the Z direction over a $100 \mu\text{m}^2$ area). This is considered as a very homogeneous magnetic field. The most significant drawbacks of this configuration is that the magnetic field norm can't be changed and it will be difficult to adjust the magnetic field direction.

3.1.2.2 Helmholtz coil

In this method we used an electric 3-axis custom build Helmholtz coil in order to get the biased magnetic field. This configuration allows to create a very homogeneous and easy to control magnetic field that is also strong enough to separate the 4 NV orientations. To built this tool, we first created a simulation of a filament magnetic field, and warp it into a solenoid using MATLAB [see Figure 11]. The simulation enable us to determine the right parameters in order meet the requirements. The final design enable creating a fully controlled magnetic field, up to ~ 35 G in all 3-axis, with maximum magnetic field deviation across a $100 \times 100 \mu\text{m}^2$ of 1.5×10^{-6} . To drive these coils we used an accurate DC supplier which was controlled by a MATLAB GUI.

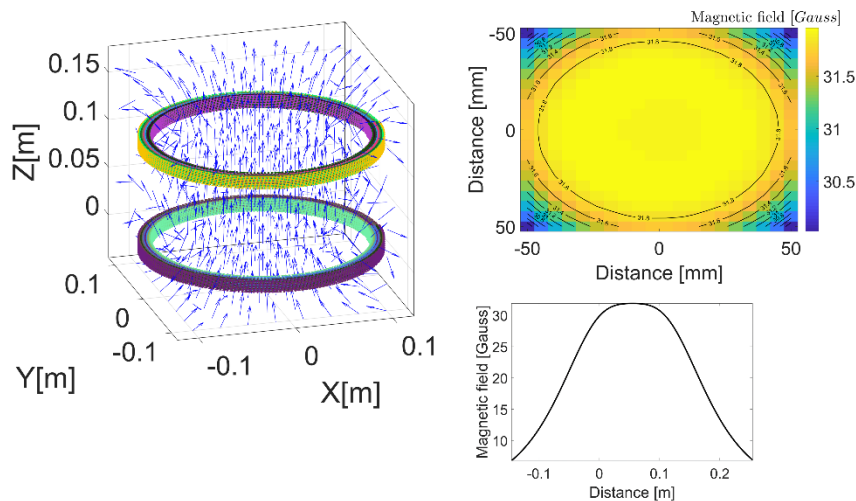
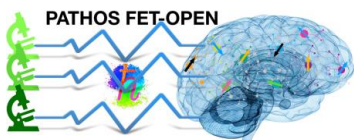


Figure 11: Magnetic field simulation of a Helmholtz coil. The colourful lines represent the electric wire filaments and the blue arrows are the magnetic field directions, left. The magnetic field magnitude cross-section perpendicular to the z axis at the middle between the coils, top right; The magnetic field magnitude along the z axis at the middle of the rings, bottom right.

3.1.2.3 Permanent magnet mounted on a 3-axis motorized stage

On this configuration we mounted a permanent magnet (model) on a motorized stage (model). The magnet attached to an adjustable arm which allows an additional manual levels of freedom. The



motorized stage controlled from the computer by a Matlab's GUI that we created. This configuration offers a medium spatial magnetic field homogeneity (maximum magnetic field deviation across a $100 \times 100 \mu\text{m}^2$ of 1.5%) and a relative simple adjustment of the magnetic field norm and direction. In our experiments we mainly work with two configuration: the first is when the magnetic field is aligned to one of the NV orientations, such that we can measure the magnetic field from one NV orientation; the second is when the magnetic field is in misalignment with all of the four NV orientations in such a way that we remove the energy degeneracy from all of the NV orientations. In this configuration we can measure the magnetic field from all of the NV orientations at the same time. To be able to get some arbitrary magnetic field we created an algorithm that can determine the magnet position and orientation such that it creates the wanted magnetic field. The algorithm runs an ODMR experiment and finds the resonant peaks' positions using a fit. Then, based on these parameters we perform an least-squares minimization. when in each cycle, the stage moves a small step in the x direction and the least-squares is calculated again, the same process repeats in the y and the z directions. Finally, the least-squares gradient is calculated, and the stage moves according to this direction until the minimum possible value is achieved.

The general expression we want to take to minimum is

$$F = (p_1 - p_{w1})^2 + (p_2 - p_{w2})^2 + (p_3 - p_{w3})^2 + (p_4 - p_{w4})^2$$

When p_i and p_{wi} is the actual and wanted position of the i^{th} NV orientation's peak in the ODMR spectrum. The parameters $p_i: i \in 1,2,3,4$ depend on each other through the NV center Hamiltonian (Equation 1). When we want to perform the magnetic field alignment, so the magnetic field will be parallel to the first orientation, without loss of generality, we need to satisfy the following conditions: we need to choose p_{w1} and $p_{w2} = p_{w3} = p_{w4} = p_3$. In this special case we can use more simple expression that doesn't depend on p_w

$$F_{\text{alignment}} = (p_1 - p_{w1})^2 + (p_2 - p_3)^2 + (p_4 - p_3)^2$$

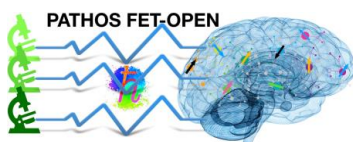
Using this expression, we do not need to calculate p_w , therefor we can avoid errors in this parameter creating from strains effects. In this way we can get the wanted magnetic alignment within several minutes with 20 steps.

3.1.3 Diamond sample

The diamond sample is a single- crystal diamond CVD-grown by Element Six. It is (100) oriented surface with edges coincide with the directions [100], [010], [001] witch define the laboratory frame denoted as (x, y, z) . This sample contains less than 5 *ppb* Nitrogen concentration, around 0.03 *ppb* NV concentration and 1.1% ^{13}C concentration. The sample surface area is $4.5 \times 4.5 \text{ mm}$ and in thickness of $300 \mu\text{m}$. This thickness was chosen to allow the collection of the luminescence of the NV layer, located on the back face, through the diamond plate, taking into account the $350 \mu\text{m}$ working distance of the microscope objective. In order to produce the wanted NV^- layer, we implanted the diamond uniformly with $^{15}\text{N}^+$ ions at energy of 10 keV and dose of $2 \times 10^{13} \text{ N/cm}^2$. After the implantation the sample were annealed at 800C° for 8 hours under a vacuumed of $7.5 \times 10^{-7} \text{ Torr}$. This process produce a $\sim 10 \text{ nm}$ -thick layer of NV centers $\sim 15 \text{ nm}$ beneath the surface of the diamond. With this dose, around 1% of the $^{15}\text{N}^+$ ions are converted to NV centers [36], which results in a surface concentration around $1.3 \times 10^{11} \text{ NV/cm}^2$ [see Figure 8].

The NV layer's depth was chosen such that it will be as close as possible to the diamond surface to increase the coupling of the NV center to the measured sample. And on the other hand, the NV's layer depth is not to shallow to avoid surface-induced noise which contribute to both decoherence and relaxation of the NV center. This level of $^{15}\text{N}^+$ ions dose was chosen In order to increase the fluorescence intensity from the NV centers' layer to decrease the readout shoot noise. And on the other hand, avoiding graphitization damage to the diamond sample, and decoherence due to NV and $^{15}\text{N}^+$ ions coupling.

3.2 Measurement protocols



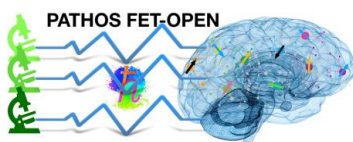
When performing vectorial magnetic field imaging, the Zeeman splitting should be found for each NV orientation. If the magnetic field being measured is at the same order as the resonance peak width in the ODMR spectrum ($\sim 400 \mu\text{Tesla}$) it will be hard to resolve the different peaks of the different NV orientations, and therefore the measurement sensitivity will be decreased. In order to receive a good measurement we lift the degeneracy between the four possible NV center orientations so we can resolve between them. To do this, we apply a $\sim 2 \text{ mTesla}$ constant magnetic field such that, the magnetic field projection is different along each NV orientation. Then, measuring three orientations from a single ODMR sweep will allow to receive the measured vectorial magnetic field information according to Equation 18. This method is relatively simple to apply and enable measurement of all the orientation with a single sweep. Alternative method is to align the biased magnetic field to one of the NV orientation separately, and measure the projection of the magnetic field along this orientation from an ODMR sweep around its resonance peak. Performing this measurement for 3 of the NV orientations will also give us the sufficient information to reconstruct the measured magnetic field. This method offers a higher coherence time, T_2^* . Decoherence in C13-rich diamonds is mainly governed by the interaction of the NV center with carbon nuclear spins that precess with a frequency $\sim 1 \text{ kHz/G}$ and nuclear-nuclear spin interactions. Both have a strong magnetic field dependence and therefore careful alignment of the magnetic field is required. Another advantage of this method is that the field norm could be relatively small (around 1 Gauss), which can be important in case the measured sample has a low magnetic coercivity.

A cw-ESR technique is employed for NV-diamond ODMR, wherein optical NV spin polarization, MW drive, and spin state readout simultaneously. Continuous 150 mW power beam at 532 nm illuminate through the opposite diamond surface containing the NV layer and polarizes the NV center into the $m_s = 0$ state. A 0 dBm MW field created by a MW antenna located close to the diamond surface enable coherently spin manipulations. Applied MWs, when tuned to resonance with the transition between the optically bright $m_s = 0$ spin state and one of the less bright $m_s = +1$ or $m_s = -1$ states, cause NV spin precession into a mixed state and a detectable reduction in the NV-fluorescence. The diamond sample was attached to a cover-slip with immersion oil, filling the air gap between the cover-slip and the diamond surfaces. We applied the immersion oil to increase both the fluorescence's collection efficiency and the effective working distance of the objective; and decrease strain effects caused by the contact of the two surfaces. The NV fluorescence pass through the diamond and the cover-slip and imaged onto the sCMOS camera using the objective. High pass and notch filters are posted right before the camera, enable light transmission wavelength of 600 – 800 nm, which allows the minimal measurement sensitivity. The fluorescence transmission band-pass have a trade-off, when increasing the band-pass, there are more contributing photons to the signal so the signal to noise ratio is getting better. On the other hand, more photons emitted from other elements (not NV center) are also being collected, and therefore the peak contrast would be smaller.

The frequency of the microwave synthesizer was swept around the resonance transition frequencies. For each frequency step, a fluorescence image was taken. The images were appended in the computer memory to form a 3D volume of data, where each element contains the value of the fluorescence for each camera's pixel and for each frequency of the sweep. This volume of data can also be considered as an image where each pixel contains an ODMR spectrum. The ODMR spectrum for each pixel was fitted to a multi-Lorentzian function (8 dips, for 2 resonance transition and 4 NV orientations) (Fig. 10 (d)). The algorithm requires initial set of parameters for the first fitted pixel. Then the entire image was fitted gradually, taking the results of the already fitted neighboring pixels as an input for the following one. Finally, the resonance positions extracted from the fit are used to reconstruct the magnetic field vector.

Calculation of the magnetic field in the lab frame was done by transforming the tetrahedral directions into Cartesian coordinates as defined in Fig. 10 (b) using the relations in equation 18. To avoid overdetermined coordinate systems we perform a calibration by applying an additional known static magnetic field along spanning set directions. Using the equations in 18 we could match each resonance dip in the ODMR spectrum to its NV orientation.

In order to get the sample magnetic field solely, we had to perform a reference measurement for each pixel in the field of view, without the sample being measured. Therefore, we first measured only the biased magnetic field and then we measured the sample magnetic field (with the biased



magnetic field as a background) while all the other system components are at the same position. The final step was to subtract the two measurements in order to get the sample magnetic field results. This procedure is needed only when the field is inhomogeneous and unknown. In case the magnetic field is homogeneous and fully controlled, we had to do a calibration only once, and then we were able to measure any sample as many times without a reference measurement, which saves us a lot of time.

We have tested and characterized three methods of ODMR measurements. In the following sections we elaborate on each method:

3.2.1 Method 1: cw-ODMR with high MW power

In this method we perform a cw-ODMR with relatively high MW power ($\Omega_R \approx 3.5 \text{ MHz}$) and high saturation value ($S \approx 0.1$) and detect the resonance transition by fitting the resulting ODMR feature to a multi-Lorentzian function using Matlab.

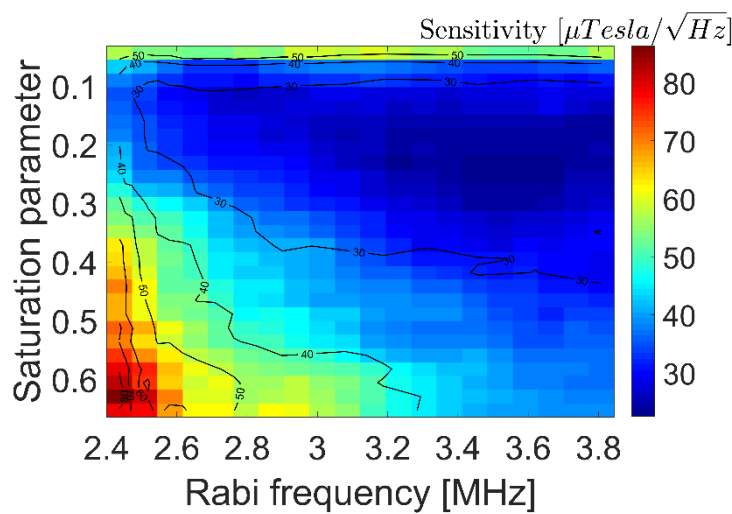


Figure 12: Two-dimensional plot of the magnetic field sensitivity of one resonant dip, achieved by the first method calculated by Equation 21 and the results of the data fitting. The solid lines correspond to isomagnetic field sensitivities. It can be seen that most sensitive point can be achieved using saturation parameter $s \approx 0.2$ and MW power $\Omega_R \approx 3.5$. The measurement was done with the following parameters: measurement time of 20 second, resolution of $270 \times 270 \text{ nm}^2$ per pixel and number of measured MW points of 100.

In order to find the sets of parameters which give the best measurement sensitivity, we checked experimentally how the sensitivity of the ODMR measurement evolves with the microwave power Ω_R and the optical pumping power s [see Figure 12]. For each microwave and optical power we performed an ODMR experiment with ~ 100 measurement points per resonance peak and total experiment time of 10 second. Using the fitting algorithm we found the peak position's uncertainty and based on Equation 21 we calculated the measurement sensitivity. Based on the result in Figure 14 we found that the best sensitivity is $23 \mu\text{T}/\text{Hz}$, for this method, obtained with the MW power of $\Omega_R = 3.5 \text{ MHz}$ and the saturation parameter of $s = 0.155$.

Using this method, we can reach magnetic field uncertainty of $\sim 2 \mu T$ after 150 sec with 270 nm spatial resolution and 35 μm field of view.

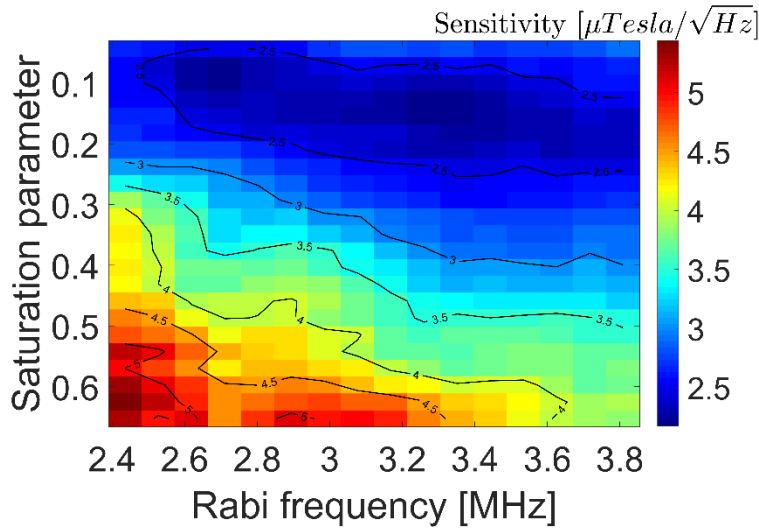


Figure 13: Two-dimensional plot of the magnetic field sensitivity of one resonant dip, achieved by the first method calculated by Equation 21 and using the maximum derivative point. The solid lines correspond to isomagnetic field sensitivities. It can be seen that most sensitive point can be achieved using saturation parameter $s \approx 0.1$ and MW power $\Omega_R \approx 3.4$. The measurement was done with the following parameters: measurement time of 20 second, resolution of $270 \times 270 \text{ nm}^2$ per pixel and number of measured MW points of 100

we have also measured the sensitivity of this method using the definition in Equation 21 by finding and calculating the maximum derivative point on the ODMR dip [see Figure 15]. Using this definition, we have managed to reproduce the theoretical sensitivity [see Figure 13].

The number of points taken per resonance dip is also a factor which affects the measurement sensitivity. In order to be in the shot noise regime ($\frac{1}{\sqrt{t_m}}$) it is necessary to take the right amount of measurement points. If the sampling is too low, the measurement is no longer a shot noise-limited [see Figure 14].

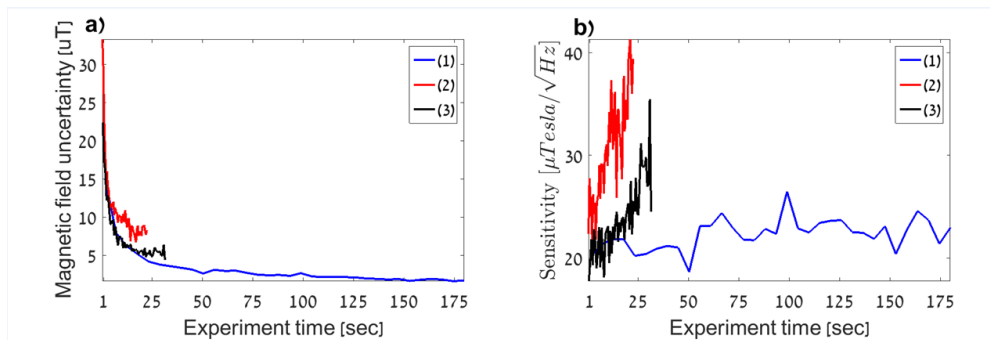
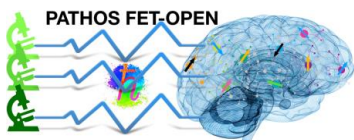


Figure 14: a) and b), the magnetic field uncertainty and sensitivity as function of the measurement time at varies number of measurement points taken for the resonance peak (98 points (1), 63 points (2) and 45 points (3)). The data obtained by the first method using Equation 21 and the results of the data fitting. The magnetic field uncertainty goes as $\frac{1}{\sqrt{t_m}}$, but this behavior is limited by the number of points.



In order to apply this method, we collected an ODMR spectrum of each pixel (corresponding to $270 \times 270 \mu\text{m}^2$ on the NV plan) after 10 sweeps and exposure time of 10 msec with 100 points per resonance peak. In addition, a reference measurement, without a MW radiation, also has been made after each frequency point measurement to reduce laser intensity fluctuations noise. Therefore, the total measurement time was $t_m = 10 \times 10 \times 10^{-3} \times 100 \times 2 = 20 \text{ sec}$. Moreover, we received a resonance peak with a contrast of 2.3% and a FWHM of 15 MHz. Based on this data, we performed a fit to a Lorentzian function with a peak position's uncertainty of $\Delta\nu_m = 0.14 \text{ MHz}$. Considering these measurement parameters we could evaluate the measurement sensitivity using Equation 21, $\eta_{method1} = 23 \frac{\mu\text{Tesla}}{\sqrt{\text{Hz}}}$ with pixel size correspondence to $270 \times 270 \text{ nm}^2$ and a $35 \mu\text{m}^2$ field of view.

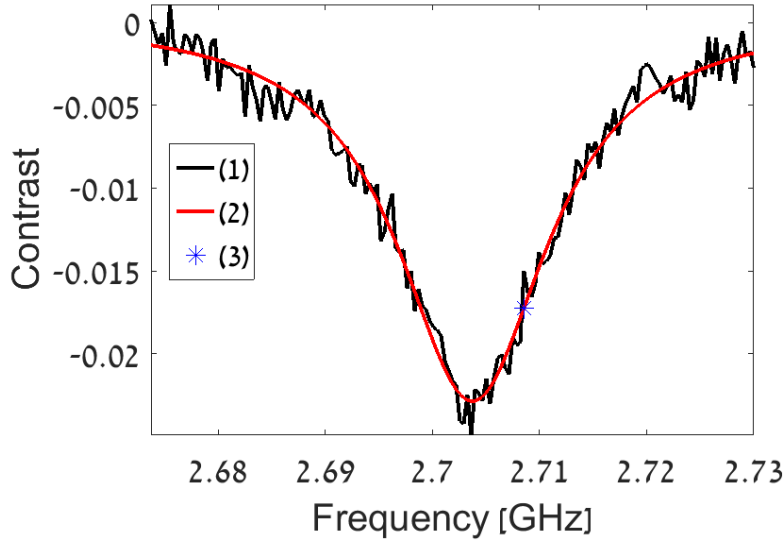


Figure 15: A typical ODMR spectrum of 270 nm pixel size (1) and a corresponding Lorentzian fit (2). In addition, the maximum derivative point is denoted by (3). The data obtained by 10 sweeps and 1000 measurement points with 10 msec exposure time for each point; saturation parameter of $s=0.155$ and a MW power of $\Omega_R=3.5 \text{ MHz}$ under a 2 mTesla biased magnetic field. Considering these parameters the peak contrast is 0.023 and the FWHM is 17 MHz. Here the resonance transition peak's position achieved by the fitting algorithm with uncertainty, $\Delta\nu_m=0.23 \text{ MHz}$

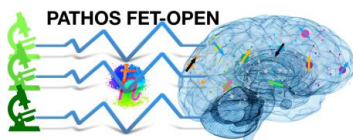
To conclude, this method is robust and simple, offers medium sensitivity and requires high biased magnetic field to lift the degeneracy between the four possible NV orientations.

3.2.2 Method 2: cw-ODMR with low MW power, sweeping with 2 MW frequencies simultaneously

In this method we performed a cw-ODMR with relatively low MW power ($\Omega_R \approx 0.1 \text{ MHz}$), sweeping with 2 MW frequencies simultaneously and low saturation value ($S \approx 0.02$). The resonant dips' locations were detected by fitting the resulted ODMR features to a multi-Lorentzian function, taking into account N15 hyperfine.

The double MW frequencies signal was produced by IQ mixer with the following input: $I = \cos(A_{\parallel})$ and $Q = \Omega_m \cos(w_m)$, where $A_{\parallel} = 2.16 \text{ MHz}$. Therefore, the outcome signal is $\Omega_m [\cos(w_m + A_{\parallel}) + \cos(w_m - A_{\parallel})]$. With this signal, the NV is driven simultaneously for both $m_l = +\frac{1}{2}$ and $m_l = -\frac{1}{2}$ states.

The outcome ODMR signal has three resonant dips, two for each hyperfine state separately and the third one, in the middle, is the combination of the two resonant transmissions. The combined dip presents a higher contrast, 1.6 times higher than the regular dips, with the same FWHM [see Figure 16].



In order to apply this method, we collected an ODMR spectrum (see example in Figure fig: 16) of each pixel (corresponding to 270×270 nm on the NV plan) after 10 sweeps and exposure time of 100 msec with 100 points per resonance peak. In addition, a reference measurement, without a MW radiation, also has been made after each frequency point measurement to reduce laser intensity fluctuations noise. Therefore, the total measurement time was $t_m = 10 \times 100 \times 10^{-3} \times 100 \times 2 = 200$ sec. Moreover, we received a resonance peak with a contrast of 0.8% and a FWHM of 2 MHz. Based on this data, we performed a fit to a Multi-Lorentzian function with a peak position's uncertainty of $\Delta\nu_m = 0.015$ MHz. Considering these measurement parameters we could evaluate the measurement sensitivity using Equation 21, $\eta_{method1} = 7 \frac{\mu\text{Tesla}}{\sqrt{\text{Hz}}}$ with pixel size correspondence to 270×270 nm and a $35 \mu\text{m}^2$ field of view.

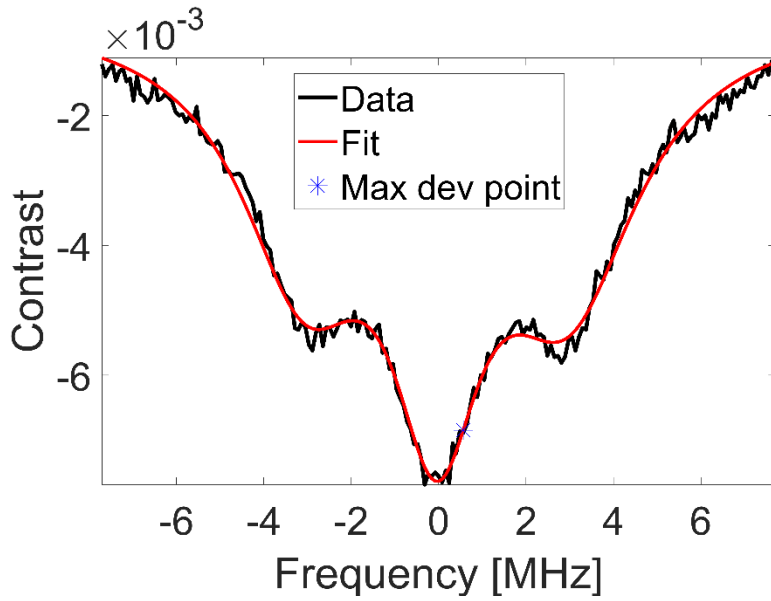


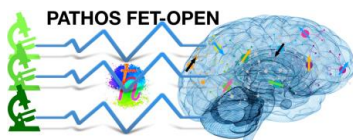
Figure 16: A typical ODMR spectrum of 270 nm pixel size (1) and a corresponding multi-Lorentzian fit (2). In addition, the maximum derivative point is denoted by (3). The data obtained by 10 sweeps and 1000 measurement points with 10 msec exposure time for each point; saturation parameter of $s = 0.02$ and a MW power of $\Omega_R = 0.1$ MHz under a 2 mTesla biased magnetic field. With these parameters, the peak contrast is 0.008 and the FWHM is 2 MHz. Here the resonance transition peak's position achieved by the fitting algorithm with uncertainty, $\Delta\nu_m = 0.015$ MHz

To conclude, this method is relatively robust and simple, offers high sensitivity and requires low biased magnetic field to lift the degeneracy between the four possible NV orientations. Therefore, this method is suitable for measuring samples with a low magnetic coercivity.

3.3 Test measurement-Magnetic image of a field formed by wire

To test our Magnetic microscope, we placed a $100 \mu\text{m}$ diameter copper wire along one of the diamond edges, at the level of the diamond surface $71 \mu\text{m}$ of the field of view [see Figure 17]. by running a DC current of 70 mA in the wire we created a constant Magnetic field of the form:

$$B_{\text{wire}} = \frac{\mu I}{2\pi r} \quad (23)$$



Where, I represents the current, $\mu = 4\pi 10^{-7} \frac{\text{Tesla}\times\text{m}}{\text{A}}$ and r is the distance from the wire.

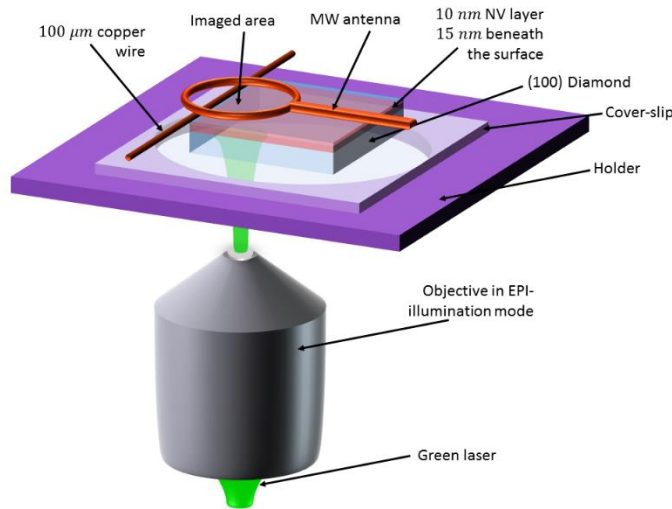


Figure 17: Scheme of the experiment. The CVD diamond plate (transparent blue) is implanted with a thin layer of nitrogen vacancy centers close to the surface (transparent red). The diamond attached to the cover-slip using immersion oil which glued to the holder. Optical pumping green laser is incident through the bottom polished side of the diamond surface using the objective in EPI mode. Coherence manipulation MW field created by a MW antenna located close to the diamond surface containing the NV layer. The NV fluorescence go through the diamond and the coverslip and imaged onto the sCMOS camera using the objective. In addition, 100 μm diameter copper wire placed along one of the diamond edges, at the level of the diamond surface 60 μm of the field of view.

When performing the magnetic field imaging, we followed the protocols presented above and they all gave consistent results; although we present only the results received from the first measurement protocol. The magnetic image result in figure 18 shows the magnetic field norm near the wire with a field of view of $30 \times 35 \mu\text{m}$ conceived by 10 sweeps with 10 msec exposure time and a 135 nm pixel size. In addition, to verify the measurement fidelity, we took a transverse cross section of the magnetic image and fitted it to Equation 23. The current and the distance evaluated based on the fit are $I_{fit} = 70 \text{ mA}$ and $r_{fit} = 71 \mu\text{m}$, which are similar to the power supply output and the distance measured optically. The data obtained from 10 sweeps with 10 msec exposure time. The measurement performed with saturation parameter of $s = 0.1$ and a MW power of $\Omega_R = 3.3 \text{ MHz}$ under biased magnetic field of 2 mTesla. The resonance peak contrast was 0.018 and the FWHM was 20 MHz.

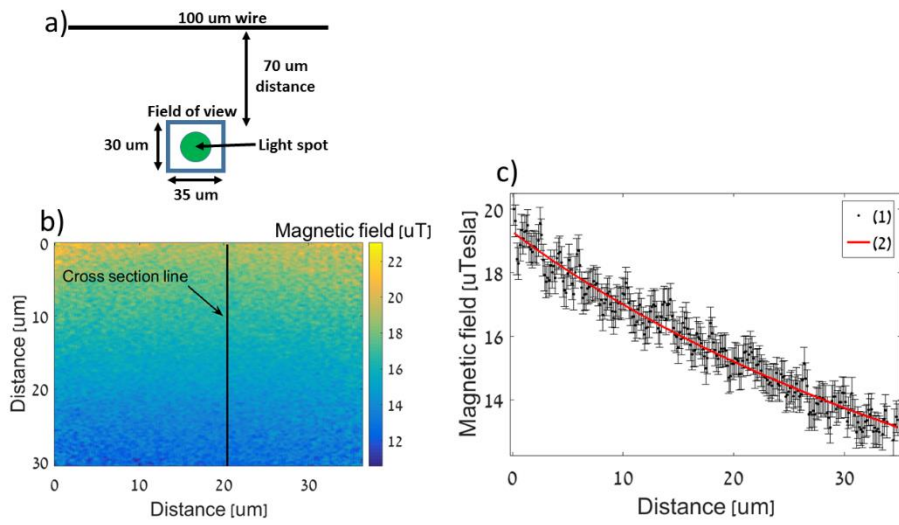


Figure 18: Magnetic field measurement. a) Top view scheme of the experiment. The 100 μm diameter copper wire placed along one of the diamond edges, at the level of the diamond surface 70 μm of the field of view which is 30×35 μm. b) 2D Magnetic field norm calculated from the raw data by the fitting algorithm. c) The magnetic field norm along the cross section marked with a black line in image b) (1) and the fit to magnetic field of an endless wire presented in Equation 23.

4 Magnetic imaging demo

We now exploit the advantages of our magnetic microscope , capable of quantitative vectorial magnetic imaging with optical resolution to explore magnetic rocks, containing magnetic grains, for paleomagnetism research [1]. We demonstrate direct imaging of the vectorial magnetic field of a single, multi-domain dendrite, as well as the measurement and calculation of the weak magnetic moments of individual grains on the micron scale. These results pave the way for future applications in paleomagnetometry, and for the fundamental understanding of magnetization in multi-domain samples.

4.1 Paleomagnetism introduction

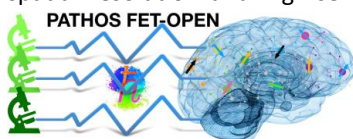
When igneous rocks in Earth's crust are formed by cooling of hot magma they acquire thermoremanent magnetization (TRM) parallel and proportional to the ambient field at the time of cooling. TRM can remain stable for millions of years preserving valuable geological magnetic information on complex long term processes, such as plate tectonic movements and formations of oceans and continents. Despite its importance, little is known on the details of how thermoremanent magnetic information is acquired and retained in rocks. Paleomagnetism, the science of studying natural magnetic information, heavily relies on Néel theory of single-domain (SD) minerals. Yet, the dimensions of rock-forming minerals typically exceed the sub-micrometric threshold size for SD. As such, TRM is mostly held by multi-domain (MD) particles rather than by SD. In the absence of a general analytical formulation for TRM in MD, there is a growing need for direct observations of natural MD magnetization. Particularly, vectorial imaging of magnetic fields generated by MD particles with sub-micron spatial resolution and micrometer scale sample-detector distance, along with high sensitivity ($\mu T/\sqrt{Hz}$), is critical for understanding the mechanism controlling the geometry and size of MD arrangements, the total moment exerted by individual natural crystals, and the stability of MD magnetic information over geological times.

4.2 Other measurement methods

There are a number of magnetic imaging techniques that have been used in paleomagnetic research in a complementary fashion: Kerr effect , Magnetic Force Microscopy (MFM), electron holography, and SQUID microscopy. Recently, a newly developed method based on nitrogen-vacancy (NV) magnetic microscopy, has been demonstrated by in the context of paleomagnetometry. NV magnetic microscopy enables direct measurements of the three components of the magnetic field vector at a constant height above the sample in a room temperature environment. It features sub-micrometer spatial resolution of quantitative data with relatively high sensitivity and simple operation.

4.3 Measuring rock samples with NV center

In this section, we explore the potential of NV magnetic microscopy in observing magnetic domains and measuring the effective dipole moment of large multi-domain arrays. We present two case studies, depicting direct quantitative, vectorial magnetic imaging of a single dendrite in the multi-domain regime, and of a pair of magnetite dendrites in the dipole regime. We finally outline the technical challenges for future use of NV-based magnetic microscopy in paleomagnetic research. Magnetization in rock samples is crucial for paleomagnetometry research, as it harbors valuable geological information on long term processes, such as tectonic movements and the formation of oceans and continents. Nevertheless, current techniques are limited in their ability to measure high spatial resolution and high-sensitivity quantitative vectorial magnetic signatures from individual

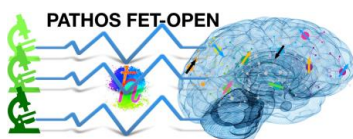


minerals and micrometer scale samples. As a result, our understanding of bulk rock magnetization is limited, specifically for the case of multi-domain minerals. In this work we use a newly developed nitrogen-vacancy magnetic microscope, capable of quantitative vectorial magnetic imaging with optical resolution. We demonstrate direct imaging of the vectorial magnetic field of a single, multi-domain dendritic magnetite, as well as the measurement and calculation of the weak magnetic moments of an individual grain on the micron scale. These results pave the way for future applications in paleomagnetometry, and for the fundamental understanding of magnetization in multi-domain samples.

4.4 Rock measurement protocol

Paleomagnetic imaging measurements were performed by placing a polished rock sample (roughly $2 \times 2 \times 1.5$ mm) on top of the diamond's surface containing the NV center layer (Fig. 10 (a)). The material we analyze was created by controlled solidification of silicate melt, simulating natural process of magma cooling in volcanic rocks. The ferromagnetic phase in the sample consists of dendrites of magnetite containing minor amounts of Mn, Mg, and traces of Al, typical to volcanic rocks, homogeneously spread in a paramagnetic silicate matrix. The size, geometry, and composition of the magnetite dendrites allows investigation of domain wall behavior in a plane parallel to a known crystallographic axis. To reduce sample topography and minimize stress effects distorting domain walls, the samples were polished down to a surface roughness of $0.02 \mu\text{m}$ using colloidal silica. We imaged the sample at two different states subsequent to the following magnetic treatment: 1) complete demagnetization state after inducing Alternating Field (AF) with a peak field of 100 mT, and 2) Isothermal remanent magnetization (IRM) after inducing a pulse of 1.5 T. The IRM field was induced in a direction nearly perpendicular to the polished surface of the sample. Yet, accurate measurement of the angle between the IRM field and the sample surface could not be precisely determined due to technical instrumental limitations. The AF treatment allowed us to investigate domain wall configurations in a "ground state" magnetization scheme, in which domains were arranged spontaneously in the absence of an ambient magnetic field. In contrast, the grain magnetization due to the strong IRM field is maximized, and the latter is used to investigate the potential of NV microscopy as a high sensitivity magnetometer.

Placement of the polished sample on the polished diamond surface resulted in a stand-off distance of a few microns, which is measured optically (by imaging the diamond surface vs. the sample surface) for each configuration. This stand-off distance translates into a spatial convolution of the measured magnetic signal on the NVs, and therefore into an effectively reduced spatial resolution (on the scale of the stand-off distance), although the inherent optical resolution limit is 350 nm (as stated above). We apply constant magnetic field, so that the magnetic field projection is different along each orientation. In this manner, all eight ODMR resonance dips are resolved (Fig. 10 (d)), and measuring three orientations from a single ODMR sweep allows us to extract full quantitative vectorial magnetic field information. We clearly identified a single magnetite dendrite using the same optical path of the fluorescence imaging microscope, and performed the ODMR measurement. Last, we performed a reference measurement excluding the rock sample, which then we used to vectorially subtract from the actual measurement. This resulted in a quantitative magnetic field produced by the rock bulk and the magnetite dendrite solely.



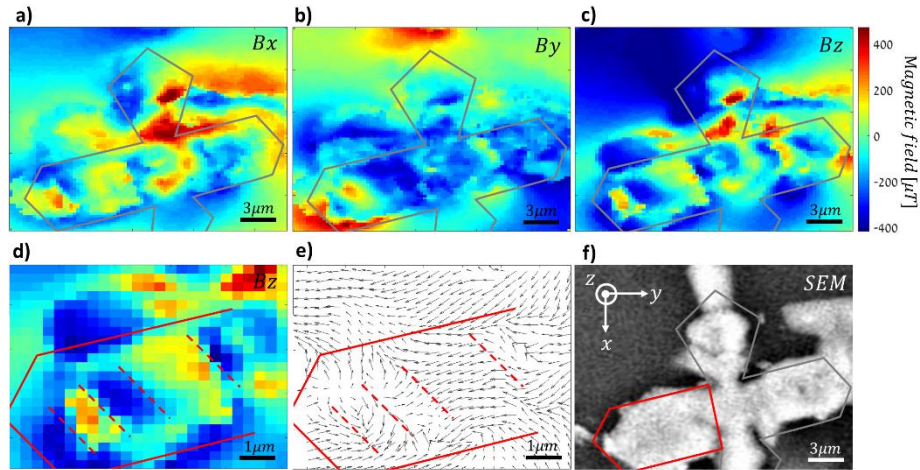


Figure 19: Magnetic field of a single magnetite dendrite in the multidomain regime after demagnetization (AF). (a)-(c) Measured magnetic field projections along the x axis (a), y axis (b) and z axis (c) within the same field-of-view. (d) Magnetic field magnification of the left branch of the dendrite along the z direction. (e) Magnetic field projection in the x-y plane of the same left branch of the dendrite as in (d). Red dashed lines represent magnetic domain walls. (f) Scanning Electron Microscope (SEM) image of the dendrite. The gray and red solid lines approximate the location of the magnetite dendrite based on the optical image received from our Wide-field magnetic imaging microscope.

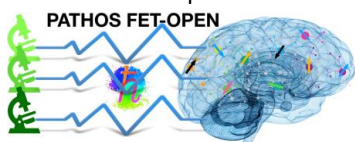
4.5 Results

4.5.1 Multi-domain measurements results

First, we present in Fig. 19 the results of the demagnetized sample at a measurement distance of $3 \mu\text{m}$ in the presence of a constant bias magnetic field of 5 mT along the $(-0.8, -0.5, -0.4)$ direction. The results show the quantitative vectorial magnetic field of a single magnetite dendrite. The branches of magnetite dendrite occur as rod-like extensions growing along magnetite $\langle 100 \rangle$ directions. The size of each individual branch of the dendrite correspond to a MD regime. The images of the magnetic field show domains with anti-parallel magnetization separated by sharp walls along the dendrite branch. The steep change in magnetic field orientation over a relatively short distance corresponds to such multi-domain behavior, and is captured by our measurement scheme (although spatial resolution is somewhat limited due to the stand-off distance between diamond and sample). The geometry, relative size, pattern, and directions of the domains are similar to those observed using MFM.

4.5.2 Dipole measurements results

Second, we present the results of a different, smaller particle after inducing IRM field in the $-z$ direction. The measurements distance to the sample is $10 \mu\text{m}$ in the presence of a constant bias magnetic field of 2 mT along the $(0.3, 0.7, -0.6)$ direction. This distance from the sample is far enough to be in a dipole regime, i.e. observing magnetic field lines similar to those of a simple dipole. This distance is on the other hand close enough to result in relatively strong field measurements. Here we used the dipole approximation to calculate the effective magnetic moment of the particle. The magnetic moment calculation was performed based on the full vectorial magnetic images, the sensor-to-sample distance and the position of the dendrite in the x-y plane. A nonlinear fit was performed to a simple magnetic dipole, leaving the dendrite depth and the vectorial magnetic moment as free parameters. The results in Fig. 20 show the quantitative vectorial magnetic field of



two magnetite dendrites and the corresponding fit of the magnetic field assuming tilted dipoles centered under the grains. The magnetic moment of the dendrite in the upper part of Fig. 3 is $\sim 1.2 \times 10^{-11} \text{ Am}^2$ along the (0,-0.6,-0.8) direction. The direction of the dipole moment is in agreement with the direction of the applied field. Assuming a pure magnetite (saturation magnetization, M_s , of $4.8 \times 10^5 \text{ A/m}$) dendrite built from six octahedra with edge length of $3.2 \mu\text{m}$ the saturation magnetization of a half dendrite, as the one shown in Fig. 3, is $2.2 \times 10^{-11} \text{ Am}^2$. It is reasonable to assume that the IRM is about half of the saturation magnetization, which result is magnetic moment of $1.1 \times 10^{-11} \text{ Am}^2$, very similar to the best-fitting dipole in Fig. 20 (d-f).

In both measurements, to separate the paramagnetic magnetization of the silicate matrix from the ferromagnetic effect, we measured the magnetic field of the matrix away from the magnetite

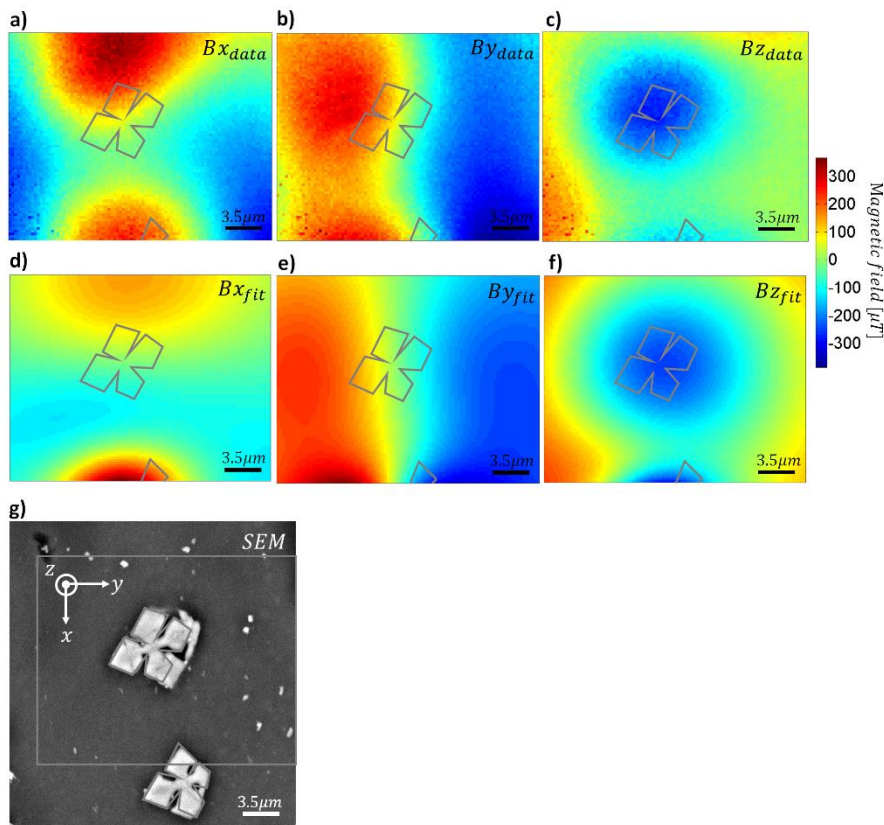


Figure 20: Magnetic field of magnetite dendrites in the dipole-dominated regime. (a)-(c), Measured magnetic field projections along the x axis (a), y axis (b) and z axis (c) within the same field-of-view. (d)-(f), Simulated magnetic field projections along the x axis (d), y axis (e) and z axis (f). (g), Scanning Electron Microscope (SEM) image of the dendrite (the magnetic images' field of view is denoted by the gray square). The gray solid lines approximate the location of the magnetite dendrite based on the optical image received from our Wide-field magnetic imaging microscope.

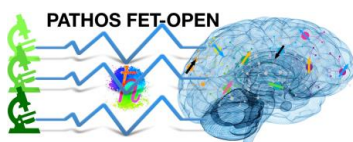
dendrite (this field is not zero due to the finite size of the sample, inhomogeneities of the material, and contributions from ferromagnetic grains). A vectorial subtraction of this measurement from the dendrite measurement resulted in an approximation of the magnetic field of the magnetite alone. In the first result (Fig. 19), the magnetic field of the rock matrix was in a direction close to constant bias magnetic field and a magnitude of 0.2 mT. In the second result (Fig. 20), the magnetic field magnitude of the rock matrix was 1 mT along the (0.6,0.6,-0.5) direction. We expect that the discrepancy between the orientation of this field and the external field stem from field inhomogeneities and ferromagnetic effects. As detailed below, more precise measurements in the future will utilize a 3D Helmholtz coil configuration, affording better field homogeneity and a clearer separation between paramagnetic and ferromagnetic effects.

4.6 Future capabilities and applications

In the demonstrated measurement modality we were limited by our control over the 2 mT bias magnetic field. The bias field exerts a paramagnetic effect on silicates, and can distort magnetic domain configuration in grains with low coercive field. We have solved this problem by adding 3D Helmholtz coils, which allow precise control over the vectorial bias field for the measurements planned in this project. We expect to be able to perform measurements with bias magnetic field smaller by approximately an order of magnitude (~ 0.5 mT), as well as to reverse the direction of the bias field in order to separate paramagnetic and ferromagnetic effects.

Moreover, we have improved our NV magnetic imaging system with enhanced, layered diamond samples, as well as with a stronger, more stable excitation laser. We characterize our current DC sensitivity at approx. $\sim 200 \frac{nT}{\sqrt{Hz}}$.

We expect this system to be a versatile, general-purpose platform for developing novel sensing and control schemes, and for demonstrating magnetic measurements in various contexts, as proposed in this project.



5 Reference

- [1] E. Farchi, Y. Ebert, D. Farfurnik, G. Haim, R. Shaar, and N. Bar-Gill, *SPIN* **07**, 1740015 (2017).

